Science Advances
AAAS

Supplementary Materials for

Observation of nonvanishing optical helicity in thermal radiation from symmetry-broken metasurfaces

Xueji Wang *et al.*

Corresponding author: Zubin Jacob, zjacob@purdue.edu

Sci. Adv. **9**, eade4203 (2023)
DOI: 10.1126/sciadv.ade4203

This PDF file includes:

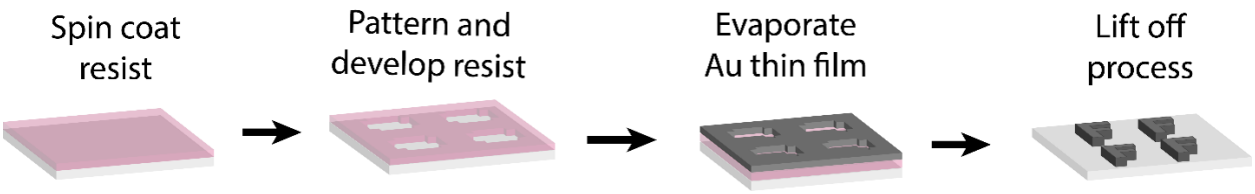

Figure S1: **Schematic of the fabrication process.** The F-shape meta-atoms are first written to the spin-coated PMMA 950 A4 resist using electron beam lithography. After the resist is developed, 120nm Au is deposited on the patterned resist using an e-beam evaporator. Finally, the metasurface is created in the lift-off process, where the excess resist is removed with acetone.

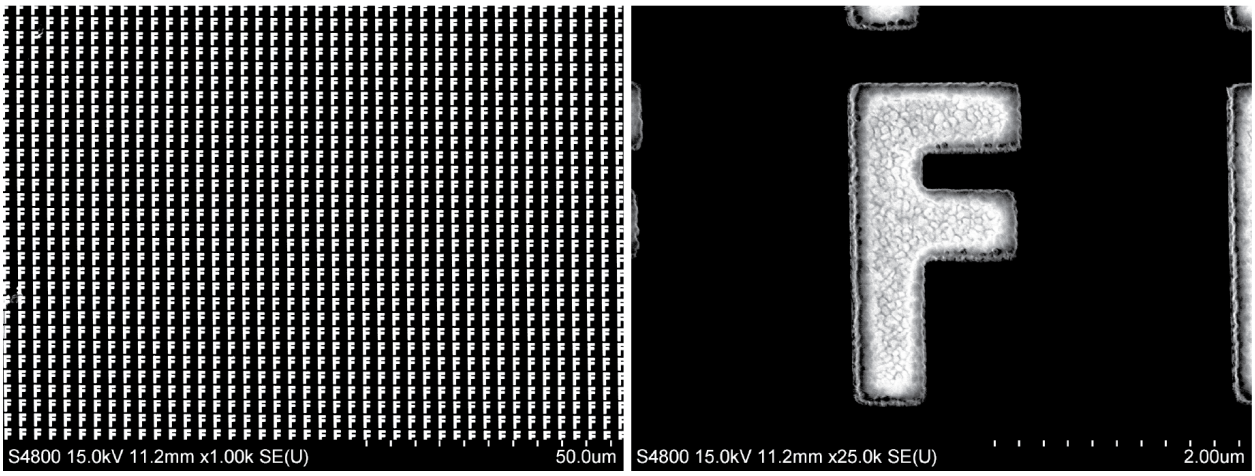

Figure S2: **Scanning electron microscopy (SEM) images with different magnification**. The large area uniformity of the metasurface (left) and the high quality of the fabricated meta-atoms (right) are demonstrated.

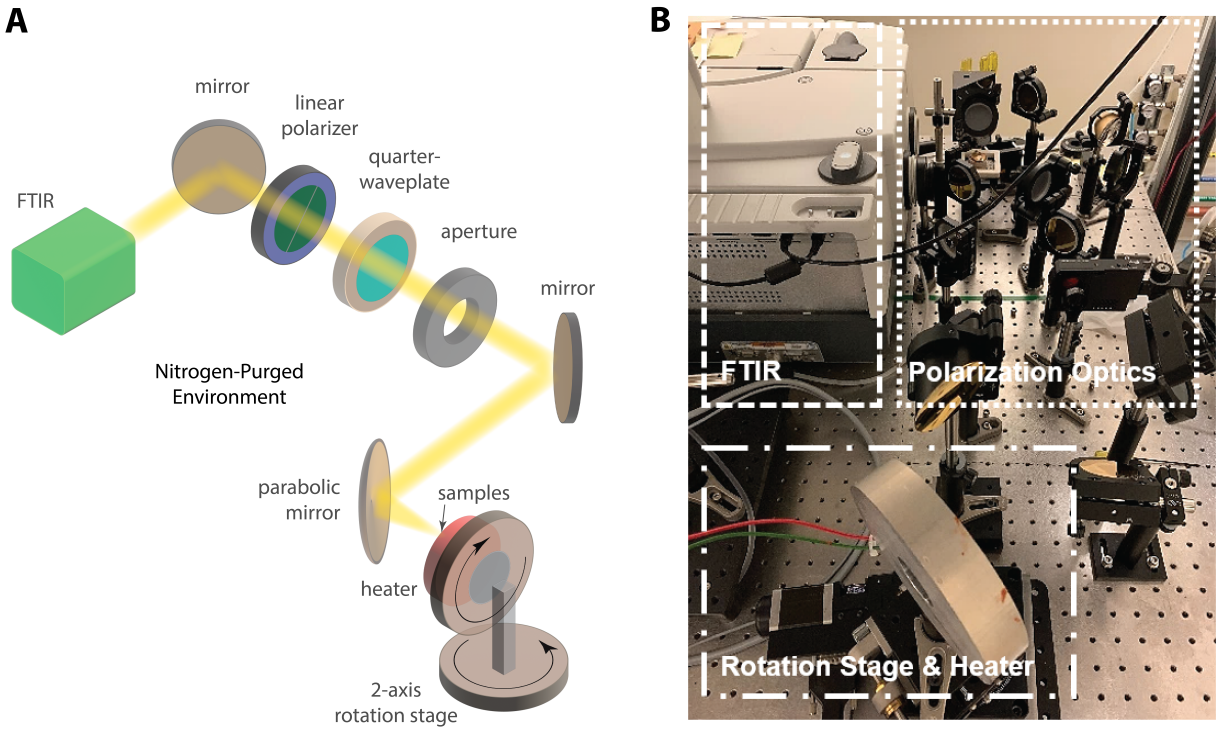

Figure S3: **Schematic (A) and optical image (B) of the spin-polarized angle-resolved thermal emission spectroscopy (SPARTES) setup.**

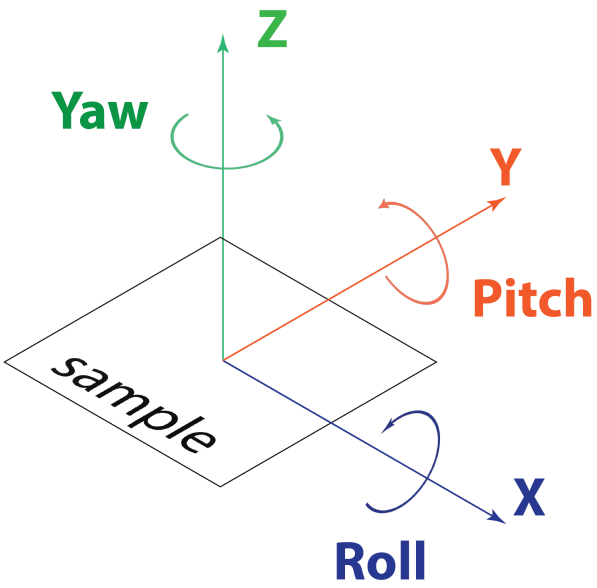

Figure S4: **Schematic demonstrating the rotational axes of the sample stage.** We note a subtle difference in our system compared with conventional angle-scanning setups. Assuming the sample sitting on the XY-plane and the collection path fixed along the Z-axis, the different momentum vectors are conventionally mapped by adjusting the Pitch for k_x and the Roll for k_y, as well as their combinations. Here, for the system's simplicity, we use the rotation options for adjusting the Pitch, and Yaw. These 2 rotations still complete the momentum mapping as the aforementioned conventional setup. For example, considering mapping along k_x by adjusting the Pitch of the system, now if the Yaw is rotated by 90 degrees, by rotating the Pitch we achieve the identical translation of our structure as if we had been adjusting the Roll from the beginning. We emphasize that this only holds because we are looking at the circular polarization, and the relative orientation between the polarization elements (waveplate and linear polarizer) and the sample does not affect the results. In our current setup, the adjusting range of the Yaw is 0 to 360 degrees (full circle) and the adjusting range of the Pitch is around - 80 to 80 degrees.

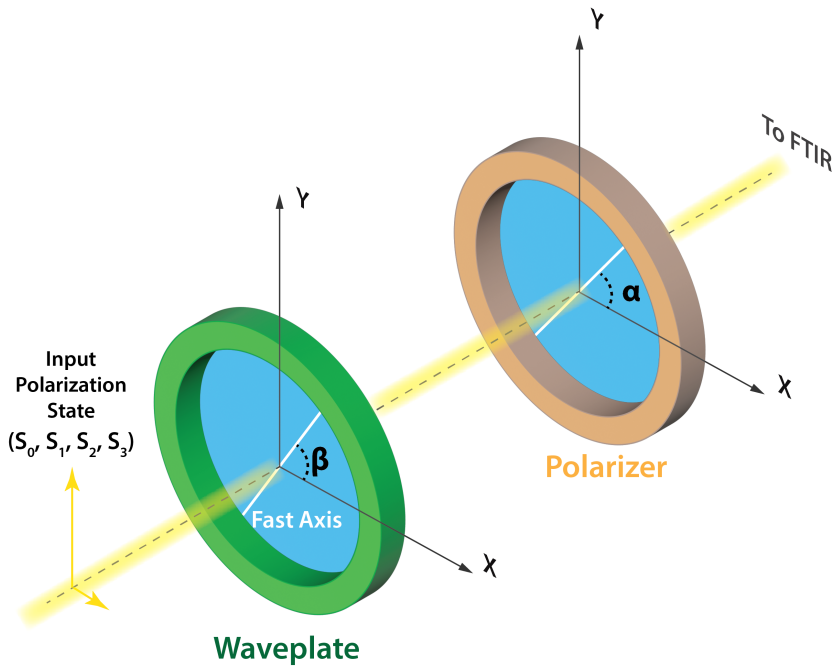

Figure S5: **Schematic of polarization characterization setup.** We use a retardation waveplate followed by a linear polarizer. The transmission axis of the polarizer is at an angle α to the x-axis, and the fast axis of the waveplate is at an angle β to the x-axis. The phase difference between the fast and slow axis of the waveplate is δ.

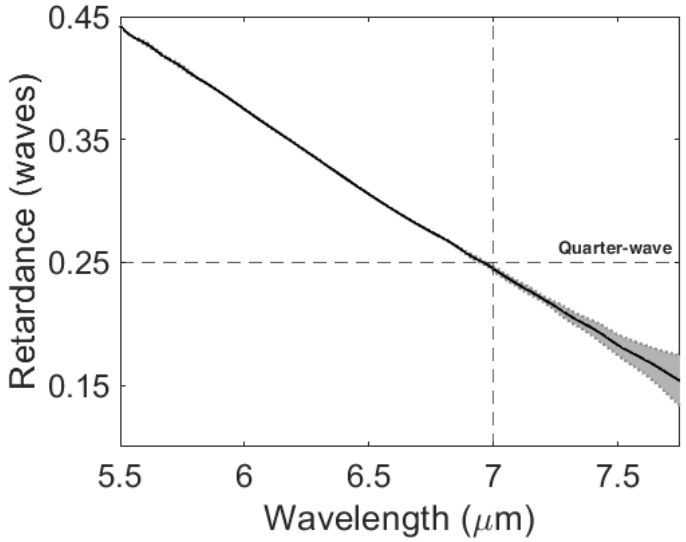

Figure S6: **Measured phase retardation of the waveplate (shaded area represents the uncertainty of the measurement)**. The waveplate has quarter-wave retardation around $7\mu m$, and a linear dispersion of retardance can be seen in the spectral region of 5.5 - $7.7\mu m$.

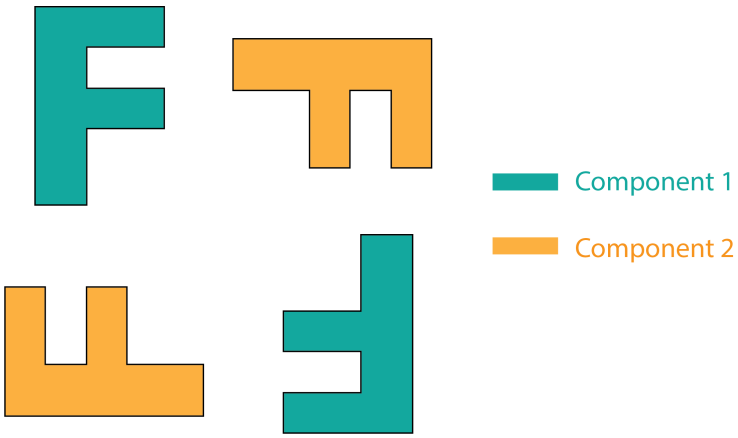

Figure S7: **Mechanism of near-zero DoCP in C4 symmetric devices**. The thermal radiation generated from the C4-symmetric metasurface can be roughly estimated by the sum of the signals from the two components (blue and orange) in the unit cell. The circular polarizations from the two components have a geometric phase difference of π because of the $\pi/2$ rotation angle between them. Thus destructive interference of the circular polarizations results in a near-zero degree of circular polarization.

Temperature Dependence

Our calibration approach requires the emissivity of the sample to be temperature-independent in the temperature range of measurements. To show this is indeed true in our experiments, we plot the raw thermal radiation signal (for LCP) at different temperatures (373.2K – 493.2K) in Figure S8. No substantial spectral shift or broadening can be observed in the resonant spectral features.

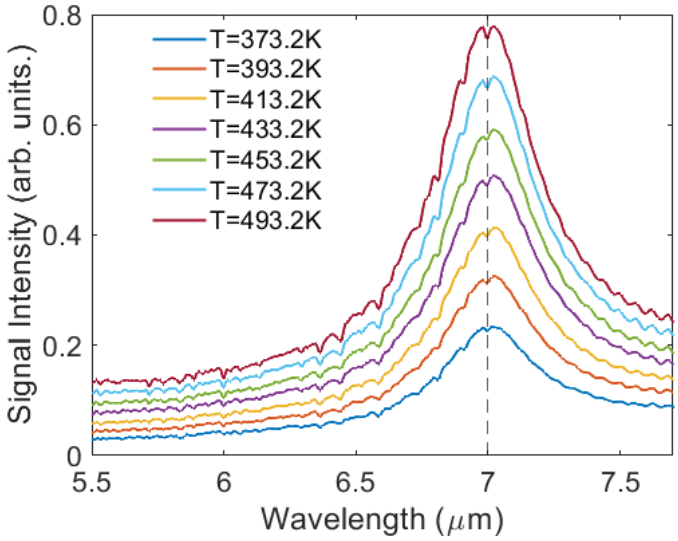

Figure S8: **Temperature dependence of the thermal radiation signal.**

To quantitatively demonstrate this, we select four different wavelengths ($5.5\mu m$, $6\mu m$, $6.5\mu m$, and $7\mu m$) and plot the signal intensity versus the blackbody radiation intensity (Figure S9). As shown in the main text, the equation for extracting emissivity is

$$e_{\tilde{\nu}}^{\alpha\theta} = \frac{S_{\tilde{\nu}}^{\alpha T_1 \theta} - S_{\tilde{\nu}}^{\alpha T_2 \theta}}{Z_{\tilde{\nu}} \left(B_{\tilde{\nu}}^{T_1} - B_{\tilde{\nu}}^{T_2} \right)} \tag{1}$$

where e is the emissivity; S is the signal intensity; Z is the response function of the system; and B is the blackbody radiation intensity calculated by the Planck's Law $B_{\tilde{\nu}}^{T} = 2hc^2\tilde{\nu}^3 \frac{1}{e^{hc\tilde{\nu}/(k_B T)}-1}$. The slope of the $S-B$ curves corresponding to the product of emissivity and the response function ($e \cdot Z$) at each specific wavelength. We show the measured sig-

nal is indeed increasing linearly with blackbody intensity (R-squared values > 0.98), which proves that the emissivity e is constant in this temperature range. We can also infer that no substantial permittivity change is occurring in our devices.

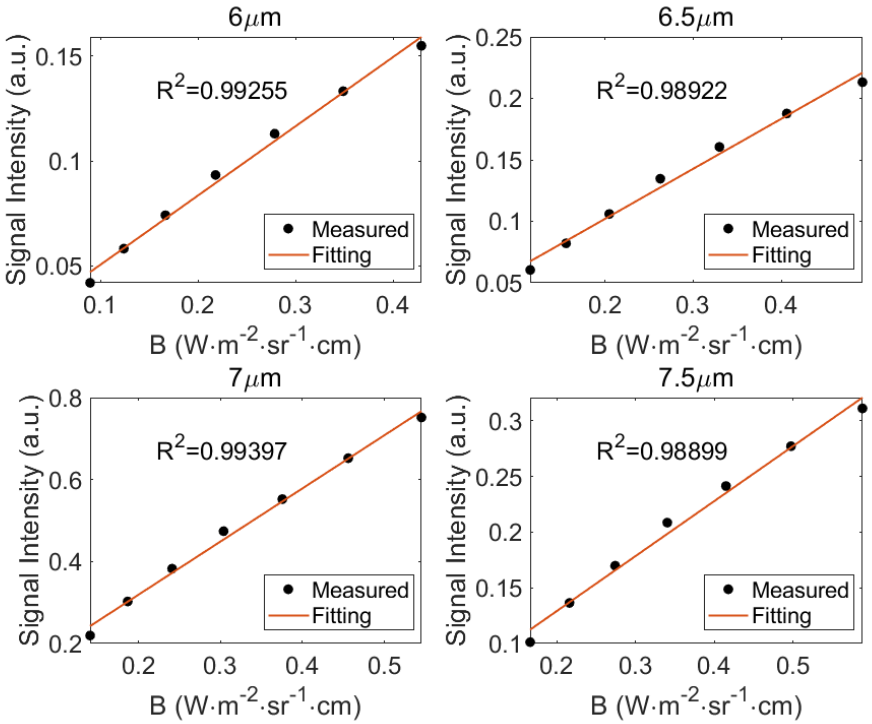

Figure S9: **The signal intensity S as a function of blackbody radiance B**. The linear relation between S and B showing that the thermal emissivity is not changing with temperature.

Energy-Momentum Dispersion

In the main text, we discuss the energy-momentum dispersion where the thermal photon momentum is along the x-axis. Here, we show the dispersion map with photon momentum along the y-axis. The experimental measurement is plotted in Figure S10 (E) to (H) and show good agreement with simulations (Figure S10 (A) to (D)). Similarly, lifted spin degeneracy (E, F), symmetric averaged emissivity (G), as well as asymmetric DoCP (H) are all observed. It is worth noting that the highly spin-polarized band around 7 μm is parabolic along the k_y direction, in contrast to the dispersionless feature shown along the k_x direction. Additional data where the photon momentum is along other directions are showing in Figure S11 - Figure S14

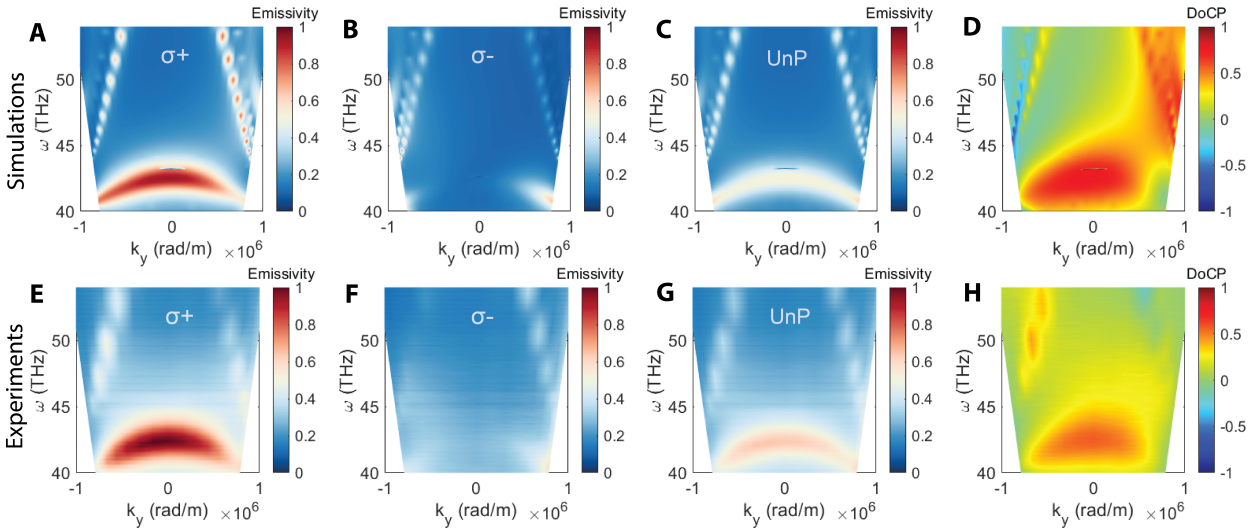

Figure S10: **Simulated (top) and measured (bottom) angle-resolved thermal radiation spectra along k_y ($k_x = 0$).** The LCP emissivity (A, E), RCP emissivity (B, F), unpolarized emissivity (C, G), and DoCP (D, H) are plotted for comparison.

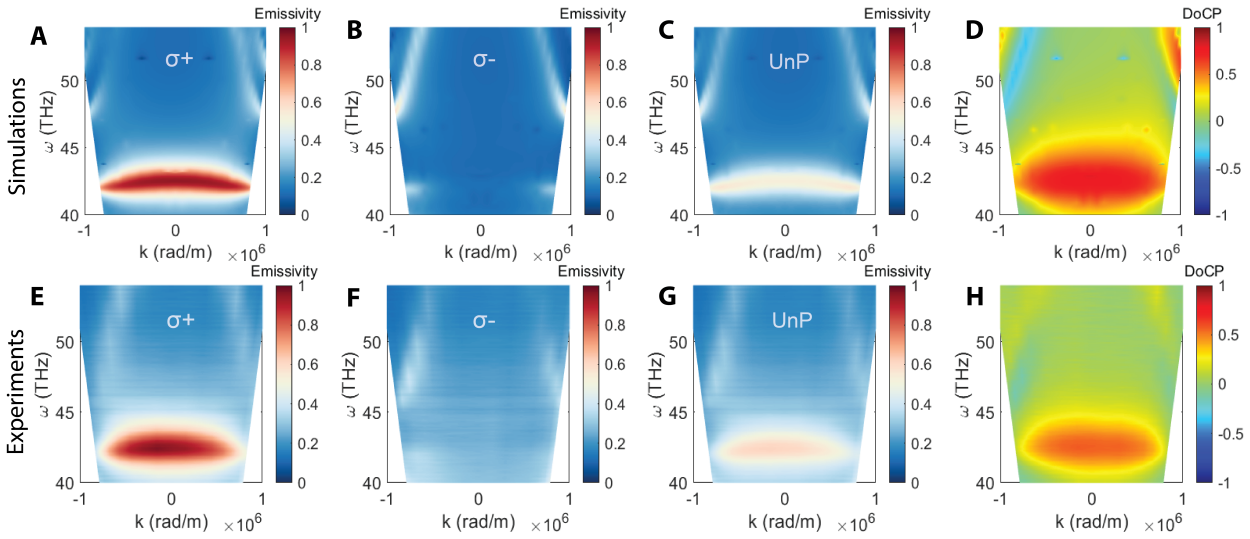

Figure S11: **Simulated (top) and measured (bottom) angle-resolved thermal radiation spectra along the azimuth angle $\phi = \pi/6$ ($k_y/k_x = tan(\pi/6)$).** The LCP emissivity (A, E), RCP emissivity (B, F), unpolarized emissivity (C, G), and DoCP (D, H) are plotted for comparison.

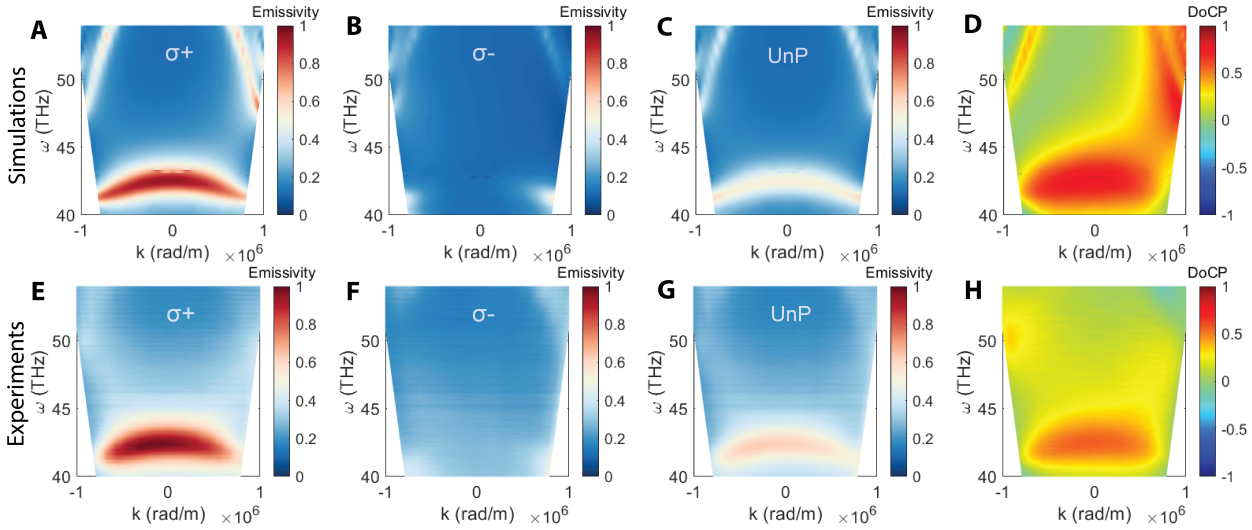

Figure S12: **Simulated (top) and measured (bottom) angle-resolved thermal radiation spectra along the azimuth angle $\phi = \pi/3$ ($k_y/k_x = tan(\pi/3)$).** The LCP emissivity (A, E), RCP emissivity (B, F), unpolarized emissivity (C, G), and DoCP (D, H) are plotted for comparison.

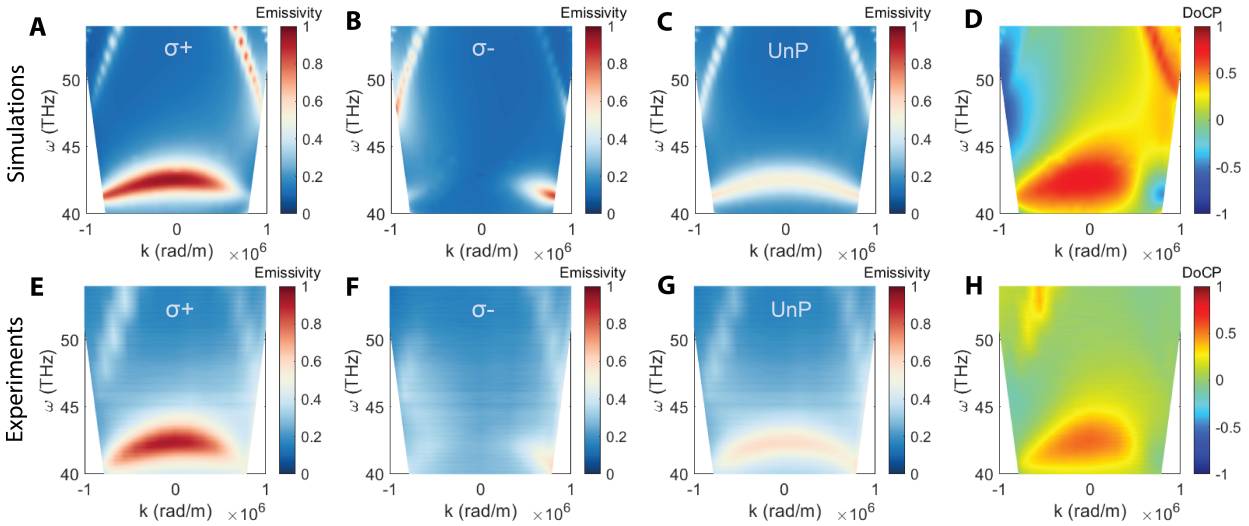

Figure S13: **Simulated (top) and measured (bottom) angle-resolved thermal radiation spectra along the azimuth angle $\phi = 2\pi/3$ ($k_y/k_x = tan(2\pi/3)$).** The LCP emissivity (A, E), RCP emissivity (B, F), unpolarized emissivity (C, G), and DoCP (D, H) are plotted for comparison.

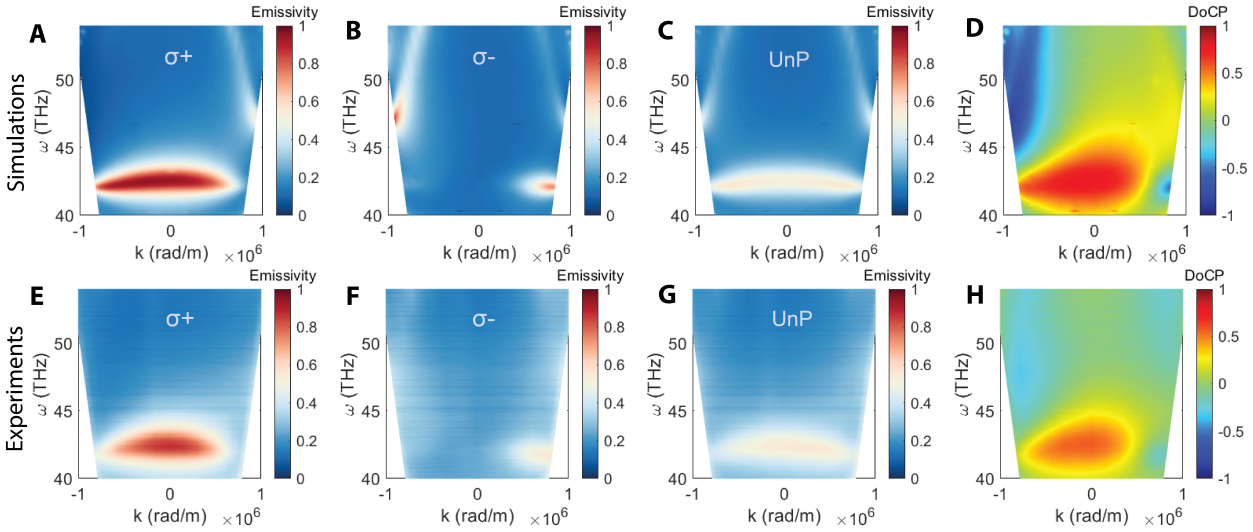

Figure S14: **Simulated (top) and measured (bottom) angle-resolved thermal radiation spectra along the azimuth angle $\phi = 5\pi/6$ ($k_y/k_x = tan(5\pi/6)$).** The LCP emissivity (A, E), RCP emissivity (B, F), unpolarized emissivity (C, G), and DoCP (D, H) are plotted for comparison.

Optical Helicity and Omnidirectionality

Optical helicity and optical spin are two different quantities describing the spin angular momentum associated with electromagnetic radiation. Optical helicity refers to the summation of the spin angular momentum (SAM) projected on wave vectors. In far-field thermal radiation, it is a direct scalar summation of the SAM value over all different directions. High optical helicity indicates the omnidirectionality of spinning thermal radiation. In contrast, optical spin considers the direction of SAM. It is an integral of the SAM vectors over the radiating hemisphere.

To show the advantage of optical helicity in quantifying the imparted angular momentum, we can consider the following thought experiment shown in Figure S15, where a perfect lens is used to collect and collimate the radiative heat signal from an emitter and transfer it to a receiver. Such an architecture is commonly adopted when collecting far-field thermal from a thermal emitter. Here, we argue that the total SAM received by the receivers is equal to the 'optical helicity' of thermal radiation. On the other hand, the quantity 'optical spin' cannot accurately describe the 'transfer efficiency' of SAM. For example:

Case 1, the spinning thermal radiation of Emitter 1 is anti-symmetric (LCP at +k directions is paired with RCP at –k direction). In this case, the net SAM received by Receiver 1 is clearly zero because there is a same amount of LCP and RCP. This fact can be captured by the zero optical helicity of Emitter 1. However, the quality 'optical spin' of Emitter 1 is not zero since LCP and RCP are associated with different k vectors (they cannot cancel out each other).

Case 2, we can also imagine a specific angular distribution of photon spin, as shown in the figure. The geometric vector summation results in a zero optical spin. However, the SAM transferred to Receiver 2 is clearly not zero because there is more RCP than LCP ($\sigma_- > \sigma_+$) in different directions.

As a result, the optical helicity is a well-suited quantity to describe the efficiency of imparting spin angular momentum via far-field thermal radiation. In the main text we aim

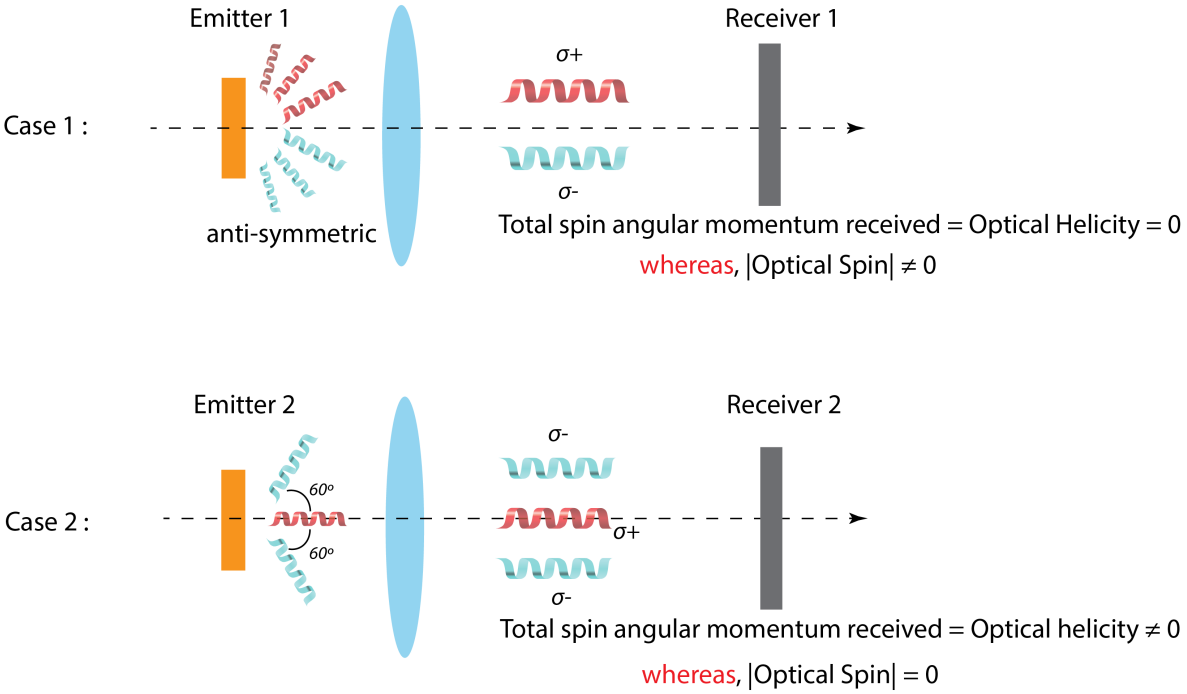

Figure S15: **The transfer of spin-angular momentum through far-field thermal radiation.** The optical helicity is a well-suited quantity to describe the efficiency of imparting spin angular momentum in this scenario.

to show that symmetry-based metasurface design provides an effective platform to control the angular distribution of photon spin in far-field thermal radiation. We choose optical helicity as it is a simple scalar value and is able to evaluate the imparted SAM in the far-field spinning thermal radiation in most cases.

Additionally, as optical helicity is directly connected to the omnidirectionality of spinning thermal radiation, we argue that omnidirectionality and high optical helicity are also highly desired in practical applications. Omnidirectionality means a wider illuminating range or field of view in cases where the metasurface is used as a light source. Here, we provide an example of practical applications to demonstrate the advantage. Considering the scenario shown in Figure S16, where the metasurface is used as a passive beacon for remote detection. The spinning thermal radiation provides a high contrast because the radiation from environmental objects has no spin textures. Omnidirectionality is highly advantageous in such cases because it means the spinning thermal radiation can be detected in a wider range.

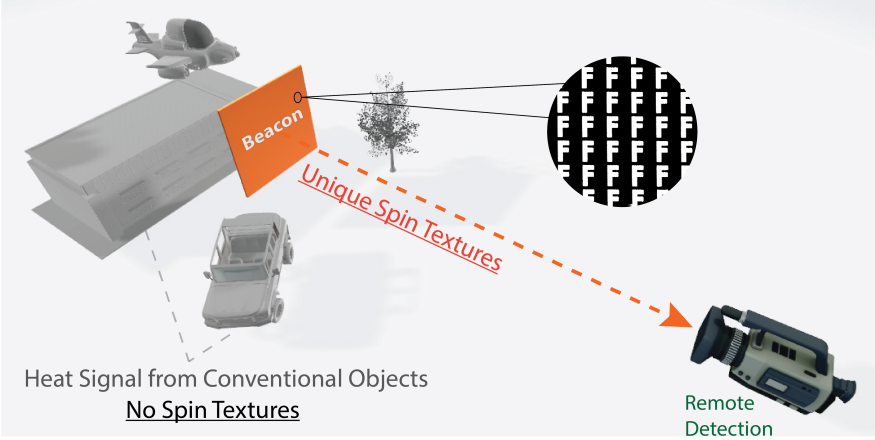

Figure S16: **Symmetry-broken metasurface as a passive infrared beacon**. The unique spin textures of the engineered thermal emission from our metasurfaces can be exploited as high-contrast infrared beacons in outdoor environments, as the background thermal emission from other natural objects is highly incoherent without any spin textures.

Optical Helicity of Symmetry-Broken Metasurfaces

In the main text, we show the optical helicity H is non-vanishing in the designed dispersionless energy band around 7μm (ω=42.8 THz). When normalized by a perfect omnidirectional LCP thermal emitter, it reaches $H/H_0 = 39\%$ of the fundamental limit. Here, we compare the result with experimentally measured differential emissivity ($\sigma_+ - \sigma_-$) outside the dispersionless band in Figure. S17. The strong contrast show differential emissivity becomes substantially smaller at all other frequencies, indicating that the dispersionless band is crucial for the observation of non-vanishing optical helicity.

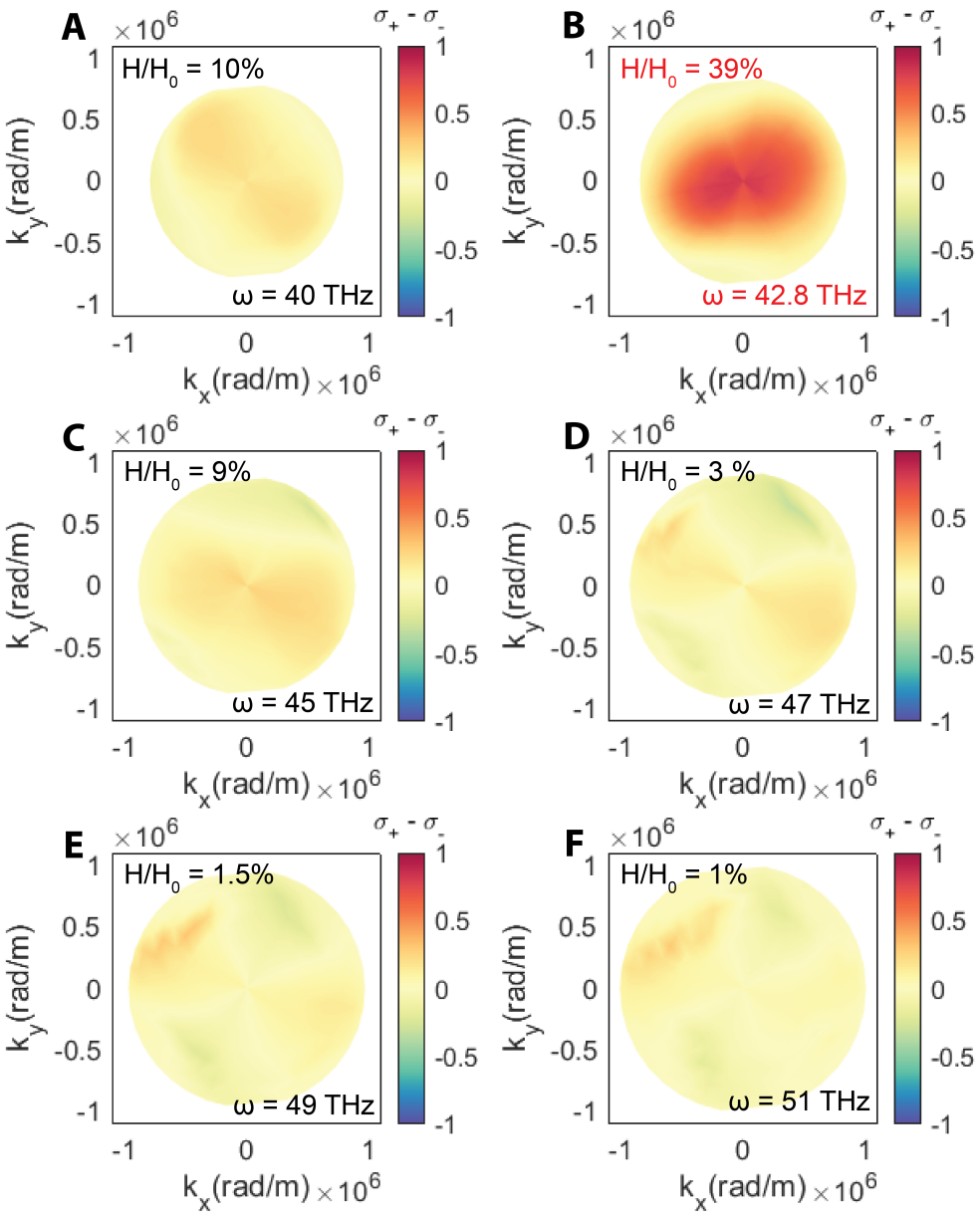

Figure S17: **Experimentally measured differential emissivity** ($\sigma_+ - \sigma_-$). The data is plotted at ω=40 THz (A), ω=42.8 THz (B), ω=45 THz (C), ω=47 THz (D), ω=49 THz (E), ω=51 THz (F), respectively. The optical helicity becomes substantially smaller outside the dispersionless band.

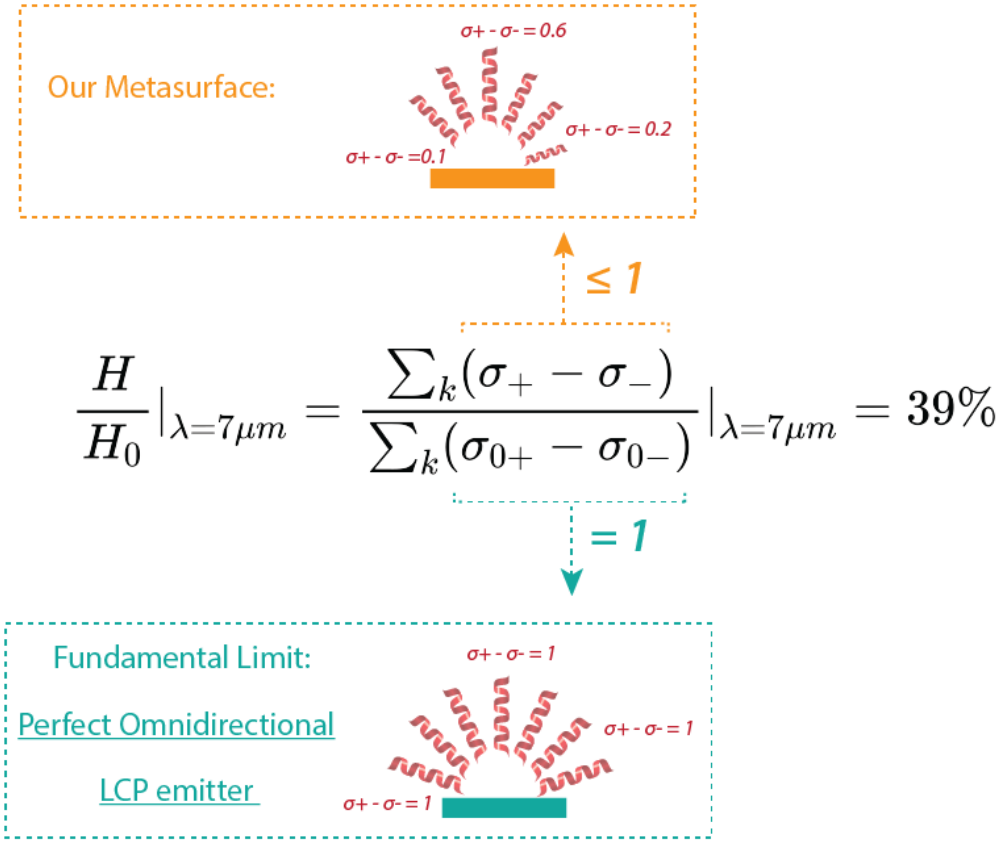

Figure S18: **The fundamental limit of optical helicity**. To quantitatively describe the optical helicity obtained in our design, we normalize the optical helicity H of our metasurface (top) by the fundamental limit H_0, i.e. the optical helicity of a perfect ominidirectional LCP emitter (bottom). We show that H/H_0 reaches 39% at the wavelength of the dispersionless band (7μm).

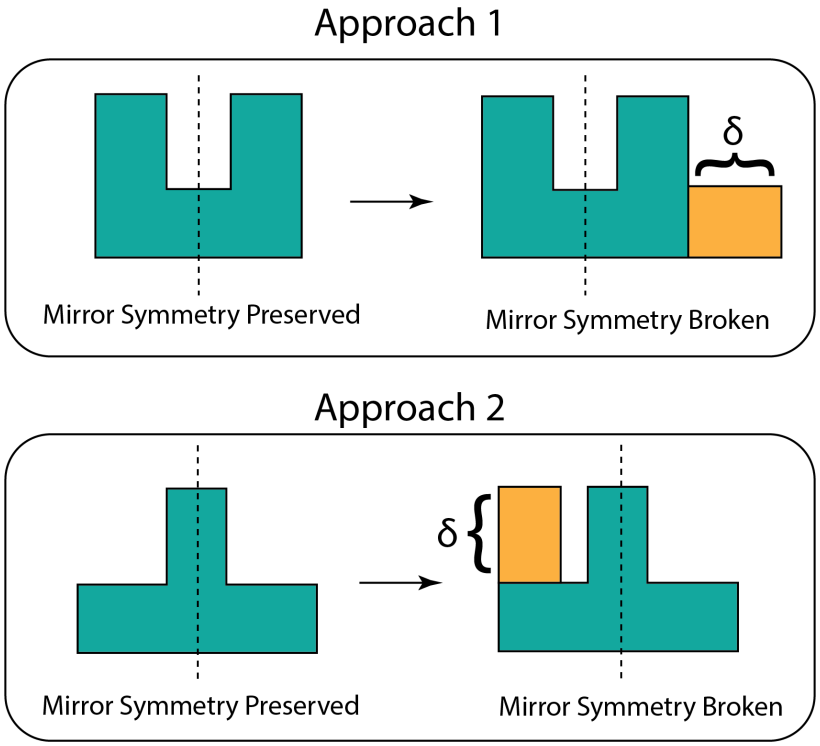

Figure S19: **Two alternative approaches to construct the F-shape meta-atom**. The meta-atoms can be considered as mirror-symmetric resonators (green) with perturbative segments (orange) breaking the mirror symmetry. Tuning the geometric parameter δ of the perturbative segments can effectively change the quality factor and the degree of the circular polarization of the resonance.